Response of the tectonically erosive south Peruvian forearc to subduction of the Nazca Ridge: Analysis of three-dimensional analogue experiments

Andrea Hampel,[1] Juergen Adam,[2] and Nina Kukowski

GeoForschungsZentrum Potsdam, Potsdam, Germany

Received 16 September 2003; revised 30 May 2004; accepted 8 July 2004; published 4 September 2004.

[1] The collision zone of the obliquely subducting Nazca Ridge and the erosive Peruvian forearc is characterized by enhanced tectonic erosion, normal faulting, forearc uplift, and a minor indentation. We apply two three-dimensional sandbox experiments monitored by an optical particle imaging velocimetry system to decipher the spatial and temporal evolution of forearc deformation. During oblique convergence the rigid model ridge causes a wave of uplift followed by subsidence to shift along the forearc. By varying the strength of the analogue material we demonstrate that the forearc response to ridge subduction, in particular the amount and rate of uplift and wedge indentation, is controlled by the mechanical strength of the forearc. The model using the high-strength material yields results more compatible with the geological record of the Peruvian forearc. First, the modeled amount of uplift scales to ~1.2 km in nature, which agrees with ~1.0 km of uplift recorded by marine terraces. Second, the calibrated model uplift rate of 0.9 km/Myr is similar to the natural rate of ~0.7 km/Myr. Third, the development of normal faults above the model ridge is in accordance with the style of faulting above the Nazca Ridge. Finally, oversteepening of the uplifted wedge and local slope failure, as observed in the experiment, has also been identified off southern Peru. A comparison between the erosive Peruvian and accretive margins emphasizes that the style of ridge-induced deformation depends on the forearc strength and crustal structure, which in turn are controlled by the long-term evolution of the margin's mass transfer regime. *INDEX TERMS:* 8020 Structural Geology: Mechanics; 8107 Tectonophysics: Continental neotectonics; 8150 Tectonophysics: Plate boundary—general (3040); 8194 Tectonophysics: Instruments and techniques; 9360 Information Related to Geographic Region: South America; *KEYWORDS:* ridge subduction, erosive forearc, 3-D analogue modeling, Peruvian margin, Nazca Ridge, particle imaging velocimetry. **Citation:** Hampel, A., J. Adam, and N. Kukowski (2004), Response of the tectonically erosive south Peruvian forearc to subduction of the Nazca Ridge: Analysis of three-dimensional analogue experiments, *Tectonics*, *23*, TC5003, doi:10.1029/2003TC001585.

1. Introduction

[2] The Peruvian convergent margin, where the submarine Nazca Ridge subducts obliquely beneath the South American continent, represents a first-order example that allows to study the response of a forearc system to the subduction of such an asperity on the downgoing oceanic plate (Figure 1) [*Kulm et al.*, 1981; *Suess et al.*, 1988; *Hsu*, 1992; *Macharé and Ortlieb*, 1992; *Hagen and Moberly*, 1994; *von Huene et al.*, 1996; *le Roux et al.*, 2000]. The geological record of the Peruvian forearc provides a suite of indications of the Nazca Ridge's impact on the margin since it entered the trench in central Peru in the Middle Miocene (Figure 1) [*Hampel*, 2002]. During its subsequent southward migration along the plate boundary, the ridge caused pronounced uplift in the forearc as evident from the temporal evolution of sedimentary facies distributions on- and offshore [*Suess et al.*, 1988; *Resig*, 1990; *le Roux et al.*, 2000]. At the present collision zone, Quaternary marine terraces have been used to constrain the amount, rate and distribution of ridge-induced forearc uplift [*Hsu*, 1992; *Macharé and Ortlieb*, 1992]. Another pronounced effect of the Nazca Ridge's passage is the enhancement of the long-term tectonic erosion acting on the Peruvian margin [*Clift et al.*, 2003, *Hampel et al.*, 2004]. Ridge-induced modification of the forearc stress field and the crustal structure of the collision zone have been inferred from analyses of faulting and geophysical data [*Couch and Whitsett*, 1981; *Sébrier et al.*, 1985, 1988; *Hagen and Moberly*, 1994; *Bialas and Kukowski*, 2000; *Hampel*, 2003].

[3] Here we report on two three-dimensional (3-D) sandbox experiments designed to study the temporal evolution of the erosive Peruvian margin during the subduction of the Nazca Ridge with emphasis on the amount and localization of forearc uplift and the development of faults. Two-dimensional sandbox experiments have been widely applied to study the behavior of friction-controlled accretive and erosive wedges of convergent margins which are considered to be analogous to wedges of sand or snow forming in front of a moving bulldozer [e.g., *Davis et al.*, 1983; *Mulugeta*,

[1]Now at Institute of Geological Sciences, University of Bern, Bern, Switzerland.

[2]Now at Department of Earth Sciences, Dalhousie University, Halifax, Nova Scotia, Canada.

0278-7407/04/2003TC001585

1988; *Liu and Ranalli*, 1992; *Kukowski et al.*, 1994; *Lallemand et al.*, 1994; *Storti and McClay*, 1995; *Gutscher et al.*, 1996; *Wang and Davis*, 1996; *Koyi*, 1997]. The 2-D approaches implicitly assume that the subducting plate moves perpendicular to the plate boundary. However, most of the natural subduction zones are characterized by oblique convergence of the plates [*McCaffrey*, 1992]. In this case, out-of-section material movements may become important and need to be considered by applying a 3-D model setup [*Burbridge and Braun*, 1998]. In particular, such a 3-D approach is required for modeling the subduction of elongated bathymetric highs that are commonly orientated obliquely to the convergence direction and migrate along the plate boundaries. The margin-parallel motion of a subducting ridge results in complex three-dimensional deformation patterns evolving in time that must be accounted for in order to assess the impact of an obliquely subducting ridge on a forearc system.

[4] For accretionary prisms, the effects induced by a subducting bathymetric high have been studied by 2-D and 3-D sandbox experiments [*Lallemand et al.*, 1992; *Dominguez et al.*, 1998]. In agreement with natural observations, these models show that at accretive margins, bathymetric highs indent and partly remove the accretionary wedge; in the wake of the ridge, accretion sets in again, given sufficient sediment supply from the oceanic plate [*Dominguez et al.*, 1998; *Schnuerle et al.*, 1998]. For erosive margins, no analogue models have, to our knowledge, been performed to investigate effects caused by a subducting ridge. Natural examples including the Nazca Ridge show that, unlike at accretive margins, the most pronounced effects are uplift and steepening of the forearc accompanied by enhancement of the long-term erosive regime [e.g., *Corrigan et al.*, 1990; *Gardner et al.*, 1992; *Hagen and Moberly*, 1994; *Collot and Davy*, 1998; *Clift and MacLeod*, 1999; *Ranero and von Huene*, 2000; *Clift et al.*, 2003; *Hampel et al.*, 2004]. Our 3-D sandbox models aim at detecting the main processes that act upon a tectonically erosive wedge during ridge subduction. We compare the experimental results that constrain the influence of a subducting ridge with the geological evolution of the Peruvian forearc system.

2. Geological Setting of the Peruvian Margin

[5] Plate reconstructions constrain that the Nazca plate converges with the Peruvian continental margin at spatially and temporarily variable velocity and obliquity [*Pardo-Casas and Molnar*, 1987; *Somoza*, 1998]. Since the Miocene, the Peruvian forearc system has been shaped by two dominant processes, long-term tectonic erosion and the subduction of the Nazca Ridge [*Kulm et al.*, 1981; *Suess et al.*, 1988; *von Huene and Lallemand*, 1990; *Clift et al.*, 2003; *Kukowski et al.*, 2003; *Hampel et al.*, 2004]. Long-term tectonic erosion caused an arcward trench retreat at a rate of 2.5–3.5 km/Myr since 20 Ma, as derived from geometrical reconstructions of the positions of the paleovolcanic arc, the paleotrench and a paleodepth reference surface [*von Huene and Lallemand*, 1990]. A recent study, which correlates reflection seismic horizons with age and paleobathymetry information from Ocean Drilling Program (ODP) Leg 112 cores, suggests tectonic erosion rates of 1.5–3.1 km/Myr at 11.5°S (Lima Basin) for the time interval 47–11 Ma [*Clift et al.*, 2003]. Since 11 Ma, average trench retreat rates at 11.5°S increased to 4.6–9.1 km/Myr [*Clift et al.*, 2003].

[6] The onset of this accelerated tectonic erosion coincides with the beginning of the Nazca Ridge's subduction 11 Ma ago at 11.2°S (Figure 1a) [*Hampel*, 2002; *Clift et al.*, 2003]. Since then, this 1.5-km-high aseismic ridge has migrated for 500 km southward along the margin to its current position at 15°S. Besides the enhancement of the long-term erosive regime, significant uplift of the forearc accompanies the passage of the Nazca Ridge [*von Huene et al.*, 1988; *le Roux et al.*, 2000]. At 11.5°S, paleobathymetry derived from benthic foraminiferal stratigraphy of ODP Leg 112 cores shows several hundred meters of forearc uplift followed by subsidence that occurred during the passage of the Nazca Ridge in the Late Miocene [*von Huene et al.*, 1988; *Resig*, 1990]. At the same time, the Rímac-Chíllon rivers deeply incised into the Lima coastal plain at 12°S, which again points to pronounced uplift presumably associated with ridge subduction [*le Roux et al.*, 2000].

[7] At the modern collision zone, shoaling of the water depth by 1.5 km along the sediment-starved trench axis from south of the Nazca Ridge to its crest documents the uplift of the toe of the frontal wedge by the underthrusting ridge (Figure 1b) [*Hagen and Moberly*, 1994; *Hampel et al.*, 2004]. Along the south Peruvian coast between 13.5°S and 16°S, up to 27 marine terraces between modern sea level and an elevation of 900 m reflect the vertical motion of the forearc induced by the ridge [*Broggi*, 1946; *Hsu et al.*, 1989; *Hsu*, 1992]. The lower terraces up to an elevation of 320 m yielded ages between 40 ka and >880 ka using electron spin resonance and amino acid racemization dating methods [*Hsu et al.*, 1989; *Hsu*, 1992]. An uplift rate of 0.5 m/ka has been derived from the elevation of the terrace assumed to have formed during the last interglacial at 125 ka [*Hsu et al.*, 1989; *Hsu*, 1992]. Using an alternative correlation between the multiple terraces and the peaks of the oxygen isotope curve, *Macharé* [1987] and *Macharé and Ortlieb* [1992] suggested a maximum uplift rate of 0.7 m/ka. All previous workers agree that the uplift is distributed asymmetrically with respect to the topography of the incoming ridge, with the uplift maximum of ~900 m located above the leading southern flank of the Nazca Ridge. The spatially asymmetric distribution of uplift suggests that above the trailing ridge flank the forearc experiences net subsidence.

[8] Until some few years back, the crustal structure of the modern collision zone was only constrained by one marine gravimetric and few single-channel reflection profiles [*Kulm et al.*, 1981; *Couch and Whitsett*, 1981]. Recently, a survey involving wide-angle and reflection seismic profiles as well as a 3-D gravimetric survey yielded detailed information about the submarine part of the south Peruvian forearc [*Bialas and Kukowski*, 2000; *Hampel*,

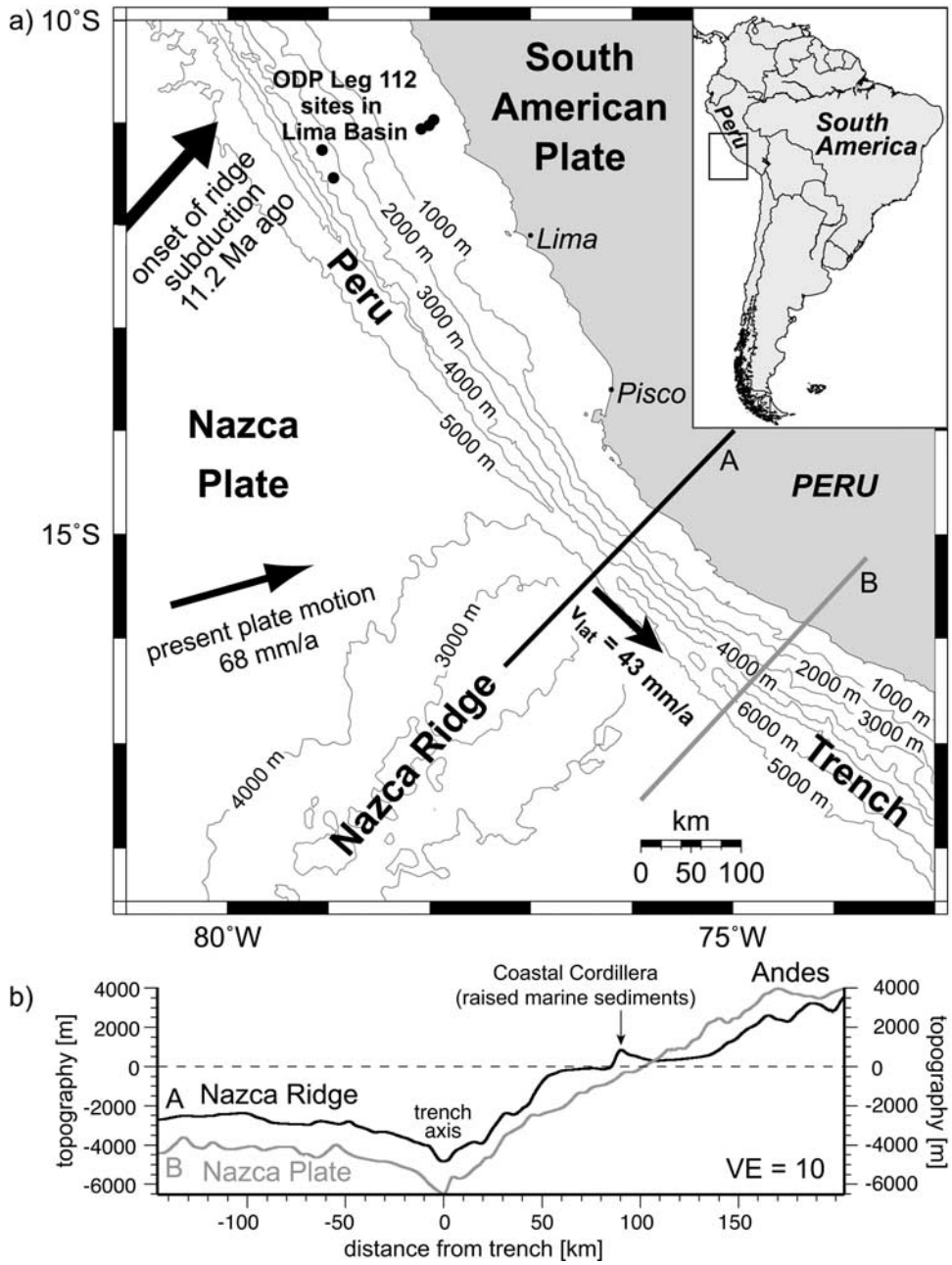

Figure 1. (a) Location map of the Peruvian continental margin with the obliquely subducting Nazca Ridge (convergence of Nazca and South American plates after *Norabuena et al.* [1998]; onset of ridge subduction and present margin-parallel velocity v_{lat} of the Nazca Ridge after *Hampel* [2002]) Gray lines marked A and B show the location of topographic profiles. (b) Topographic profiles across the Nazca Ridge (A) and the Nazca plate south of the ridge (B) illustrate that the raise of the forearc by 1.5 km. At the coast, forearc uplift decreases to ~900 m. The uplift signal from the underthrusting Nazca ridge vanishes ~50 km inland from the coast. (Topographic data by *Smith and Sandwell* [1997]).

2003; *Heinbockel*, 2003; *Hampel et al.*, 2004]. The data indicate that the forearc mainly consists of rocks with high densities (2600–2800 kg/m^3) and high seismic velocities (4.2–5.5 km/s). These crystalline rocks, which are covered by a thin veneer of sediments, extend from the coastline almost to the trench. Side-scan sonar and bathymetric images show that the Nazca Ridge neither deeply indents the frontal wedge nor induces a compressional stress regime on the south Peruvian margin [*Hagen and Moberly*, 1994; *Li and Clark*, 1994]. Instead, onshore Quaternary normal

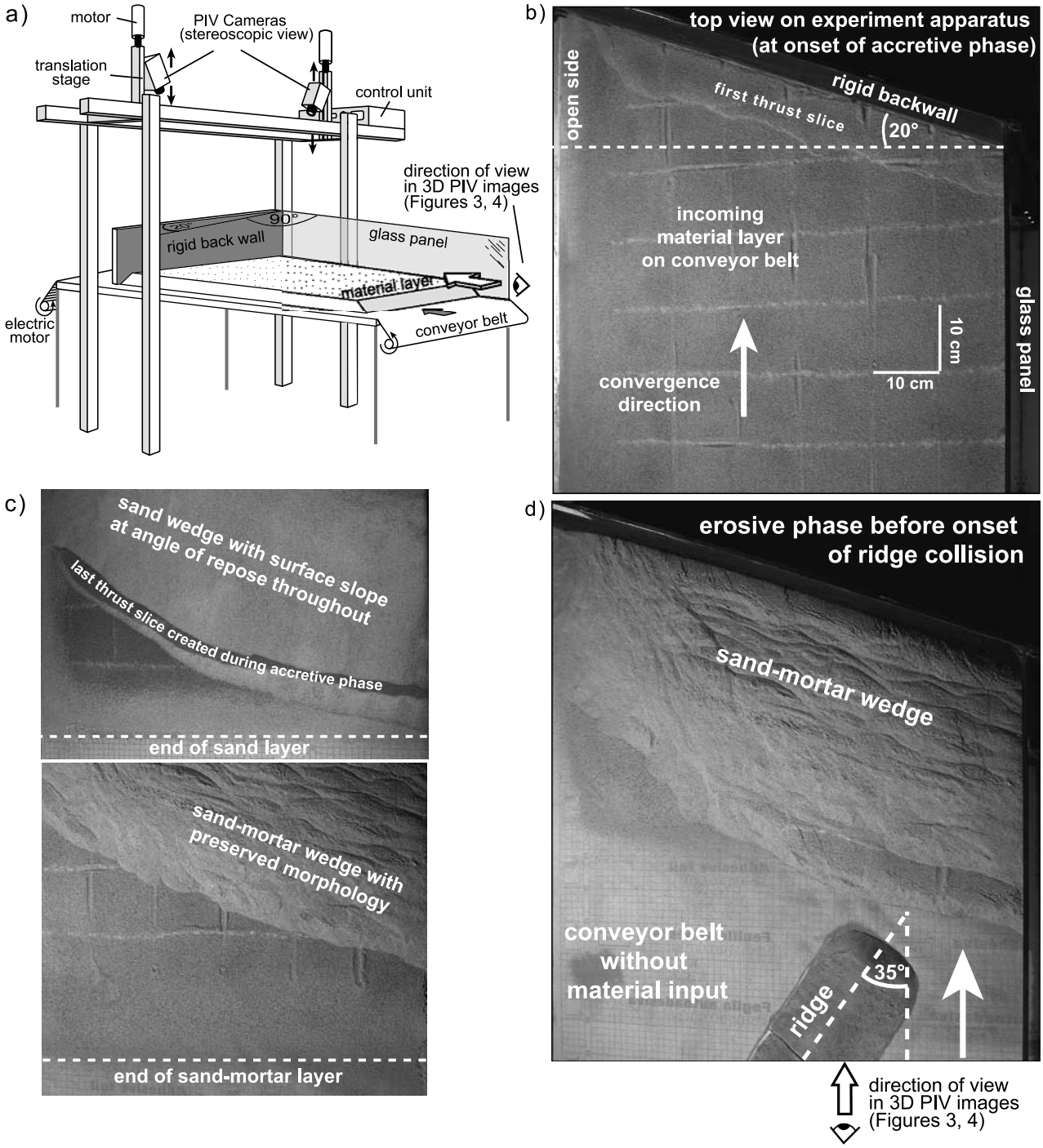

Figure 2. (a) Schematic sketch of the 3-D sandbox experiment apparatus and the stereoscopic PIV camera setup. (b) The configuration of the experiment with 20° obliquity of convergence and high basal friction of the conveyor belt reflects the setting at the Peruvian margin. In an initial model phase, a 3-cm-thick incoming material layer is accreted and forms a wedge, which is eroded in the main model phase. (c) The material input ceases and the erosive phase begins, during which the model ridge approaches the wedge with an orientation of 35° to the convergence direction like the Nazca Ridge off Peru (d). Note that the slope of the sand wedge is at its angle of repose throughout at the onset of the erosive phase, whereas the sand-mortar wedge does not exceed its critical taper.

faults indicate horizontal extension of the forearc above the ridge [*Sébrier et al.*, 1985, 1988].

3. Concept of the Analogue Experiments

3.1. Setup of the 3-D Sandbox Experiments

[9] The experimental apparatus consists of a fixed horizontal plate on which a conveyor belt is dragged underneath a rigid back wall, representing the subducting oceanic plate and the rigid part of the continental margin, respectively (Figures 2a and 2b). The rigid back wall does not allow outflux of the material to assure that the model retains a sufficient amount of material during the erosive phase before the model ridge arrives. Previous test runs showed that the sensitivity of the erosive wedge to an open or closed setting is negligible. A glass panel bounds one side of the sandbox; the other is open to allow lateral material transfer parallel to the rigid back wall (Figures 2a and 2b). The angle between the back wall and the normal on the glass panel is set to 20° according to the natural configuration off Peru (Figure 1). The conveyor belt is an adhesive foil with sprinkled sand, which is driven by an electric motor. Note, however, that the governing equations for the state of a Mohr-Coulomb wedge are independent of the convergence velocity. To allow a direct comparison to nature, the model is scaled in size, density, and cohesion with a scaling factor of $\sim 10^5$, i.e., 1 cm in the model is equivalent to 1 km in nature (for details on scaling see Appendix A).

[10] Two experiments were carried out, one with dry quartz sand (grain size < 0.63 mm) and the other using a 1:1 mixture of dry quartz sand (grain size of < 0.4 mm) and dry mortar, respectively. Measurements of the frictional properties of the two materials showed that the sand-mortar mixture is characterized by a higher internal friction than pure sand (see Appendix A and Table A1). The difference between the dynamic internal friction of both materials (Table A1) and the basal friction along their contact with the conveyor belt is sufficiently small to maintain an erosive regime, in which the basal shear zone develops as an internal basal shear zone of the wedge [cf. *Dahlen*, 1984]. Therefore the basal friction is equivalent to the dynamic stable friction of the wedge material. For both materials, the dynamic stable friction and thus the basal friction is high ($\mu_{sand} = 0.57$, $\mu_{sand\text{-}mortar} = 0.62$; see Table A1), which is agreement with the value of $\mu = 0.6$ inferred for the Peruvian margin [*Davis et al.*, 1983; *Kukowski et al.*, 1994].

[11] The analogue material is sifted 3 cm thick onto the same conveyor belt in both experiments. Both model runs begin with an accretive phase, during which the entire material input is accreted and an accretionary wedge starts to grow by the successive formation of thrust slices (Figures 2b and 2c). This procedure avoids an arbitrarily sifted wedge geometry, which could potentially influence the later stages of the experiment. After this initial phase, the material input ceases and the erosive main phase begins in order to create a setting similar to south Peru (Figure 2c). During the erosive phase, a 3-cm-high ridge, made of dried modeling clay and sprinkled with sand to minimize the contrast in friction with respect to the surrounding sand paper, is put onto the foil with an orientation of 35° to the motion direction of the conveyor belt (Figure 2d). The ridge remains undeformed during the course of the experiments, which is justified by the observation that aseismic ridges worldwide do not deform significantly during subduction beneath the forearc [e.g., *Collot and Davy*, 1998; *Schnuerle et al.*, 1998; *Hampel et al.*, 2004]. A symmetric shape with gently dipping flanks is given to the ridge in agreement with the shape of large natural aseismic ridges [*Corrigan et al.*, 1990; *Dominguez et al.*, 1998; *Gutscher et al.*, 1999; *Hampel et al.*, 2004]. The model ridge is not scaled to the dimensions of the Nazca Ridge, but is twice as high in order to exaggerate potential effects to achieve a better spatial resolution with the monitoring system. With a height of 3 cm, equivalent to 3 km in nature, the model ridge still is within the range of elevations observed at natural submarine ridges [*McCann and Habermann*, 1989].

3.2. Monitoring of the 3-D Sandbox Experiments by the PIV System

[12] In order to obtain quantitative results from our analogue models, we monitored the two experiments by a commercial high-resolution particle imaging velocimetry (PIV) system. PIV is an optical, nonintrusive method for the visualization of nonlinear flow and deformation and enables to measure the instantaneous velocities and displacements of particles in laboratory-scale models. These capabilities make PIV an ideal method for high-resolution 2-D and 3-D strain monitoring in sandbox experiments [*Adam et al.*, 2004]. In the following, the principles of PIV monitoring and processing and the specific adjustments to obtain the 3-D displacement field of a model surface are summarized.

[13] During a sandbox model run, the location of particles is recorded by time series digital images of 12 bit monochrome charged-coupled device (CCD) cameras. The displacement field between successive images is determined by adaptive multipass cross-correlation of gray-value patterns formed by groups of particles [*Fincham and Spedding*, 1997; *Scarano and Riethmueller*, 2000; *Wieneke*, 2001]. To obtain the 3-D displacement field of a model surface, a stereoscopic camera setup with two cameras, which look onto the experiment from above and take sequential stereo images, is employed (Figure 2a). The cameras are operated by the PIV software and can be moved in vertical direction automatically (translation stage in Figure 2a). For our experiments we have chosen a sample rate of 1Hz, which is sufficient to monitor the motion of the model surface. Prior to the model run, a 3-D volume calibration is performed to determine the specific mapping function of the camera setup. After the experiment, this mapping function is used to correct the recorded pairs of images for distortions and to calculate the apparent displacement (offset) resulting from the different visual angles of the two cameras. In a first processing step, the actual surface of the experiment is computed as a digital elevation model. Using this surface height information and again the mapping function, pro-

cessing proceeds with the calculation the 3-D displacement field by cross correlation of surface particle patterns in successive images. This yields the 3-D vector field for every surface element.

[14] The spatial resolution of the PIV system is determined by the distance of the cameras from the imaged object and the optical resolution of the cameras (2048 × 2048 pixels). The accuracy of the displacement vector length is better than 0.1 pixel, which translates into an uncertainty of ~0.05 mm for the experiments of this study. Apart from that, the resolution of the displacement paths of particles depends on the ability of the cross-correlation algorithm to trace particle patterns through successive images. Therefore particles of different gray-values must not move too fast in the time interval between two successive images. Successful imaging of slumping events (section 4) demonstrates that the system is robust in tracing even fast moving particles.

4. Simulating Ridge Subduction at an Erosive Margin

4.1. Experiment 1 With Pure Sand

[15] In the first experiment, pure sand was used as analogue material. The accretionary wedge that formed during the initial phase soon develops a steep surface slope owing to the high basal friction. Frequently, oversteepening followed by slumping of material occurs indicating that the angle of repose is locally exceeded [cf. *Dahlen*, 1984]. At the beginning of the erosive phase, the surface slope of the wedge is at failure throughout (Figure 2c, upper image). The thrust slices formed earlier during the accretive phase are completely covered beneath the multiple slumps.

[16] As the ridge collides with the wedge, its crest gradually indents the lower slope to a maximum of ~3 cm (Figure 3, left column). This reentrant is maintained throughout the course of the collision. The material of the wedge, which tends to move toward the open side of the experiment before the collision, is pushed upward and then aside, in the direction of the lateral ridge motion (Figure 3a, right column). Faulting of the wedge due to the underthrusting ridge is not observed, owing to frequent sliding of the sand. The ridge further steepens the slope of the wedge and triggers additional slumping often diverging above the crest of the ridge (Figures 3b and 3e).

[17] During further subduction and lateral migration of the ridge, uplift of the wedge occurs at three different areas relative to the ridge. First, with the highest uplift rates of ~0.02 cm/s above the ridge crest (Figure 3a, right column), second, in the prolongation of the ridge in the upper parts of the wedge (Figures 3c–3e, right column), and third, above its leading flank (Figures 3c–3e, right column). The maximum amount of uplift supported by the strength of the sand wedge above the ridge is small (~1 cm; not shown in figure), because the slope of the wedge is at the angle of repose and quickly adjusts by failure. The PIV image sequence shown in Figure 3 documents that areas experiencing maximum uplift shift from the ridge crest toward the leading flank of the ridge during the course of the experiment. In the wake of the ridge, the wedge subsides again (Figures 3a, 3c, and 3d, right column), accompanied by frequent sliding of the sand. As a consequence, the effects of the ridge passage are not preserved in the morphology of the slope.

[18] The monitoring of the slump events illustrates that the PIV system is capable to trace sand particles with velocities of up to ~0.6 cm/s at the used frame rate of 1 Hz. However, the frequent slumping inhibits continuous monitoring of small-scale or long-lived effects caused by the underthrusting ridge. Nevertheless, the basic mass transfer pattern during ridge subduction, with uplift along the ridge crest and above its leading flank and subsidence above its trailing edge, has been extracted from the first experiment.

4.2. Experiment 2 With the Sand-Mortar Mixture

[19] Analogous to the first experiment, the model undergoes an accretive initial phase with the formation of an imbricated wedge. However, the 1:1 sand-mortar mixture increases the slope stability because of its higher internal friction. Thus the wedge is still within the taper stability field [cf. *Dahlen*, 1984], and does not exceed its angle of repose at the end of the accretive phase (Figure 2c). As a consequence, the morphology of the wedge that developed during the accretive phase is preserved (Figure 2c, bottom).

[20] During the subduction of the model ridge, in particular during the first ~10 cm of convergence of the collisional phase, the wedge adjacent to the ridge remains largely stable, which allowed to monitor the particle displacement in great detail (Figures 4a–4h). During the first stages of the collision, the material of the lower slope is uplifted at a rate of ~0.05 cm/s and pushed aside by the ridge (Figures 4b–4d, right column). Above the leading flank of the ridge, oblique normal faults develop in the wedge (Figures 4b–4d, left column). These faults accommodate the movement of material displaced by the subducting ridge and appear to rotate about steep axes with continued subduction. The small lateral displacements along

Figure 3. Image sequence of the first experiment with pure sand showing the collision and lateral migration of the model ridge (left column) and the 3-D displacement field derived from PIV monitoring in a perspective view (right column). The viewpoint toward the wedge from behind the ridge is depicted in Figure 2a. The blue arrows in the PIV images represent the total displacement vectors (length of vectors is 20 times the displacement). The total displacement vectors are overlain on the vertical component of the displacement vector (right column; color code on model topography). Thick red and green arrows mark uplifting or subsiding areas, respectively (right column). Thin green arrows mark the parts of the slope that fail because of oversteepening (right column). In white areas without blue vectors the particles moved faster than the PIV system could trace them. See color version of this figure at back of this issue.

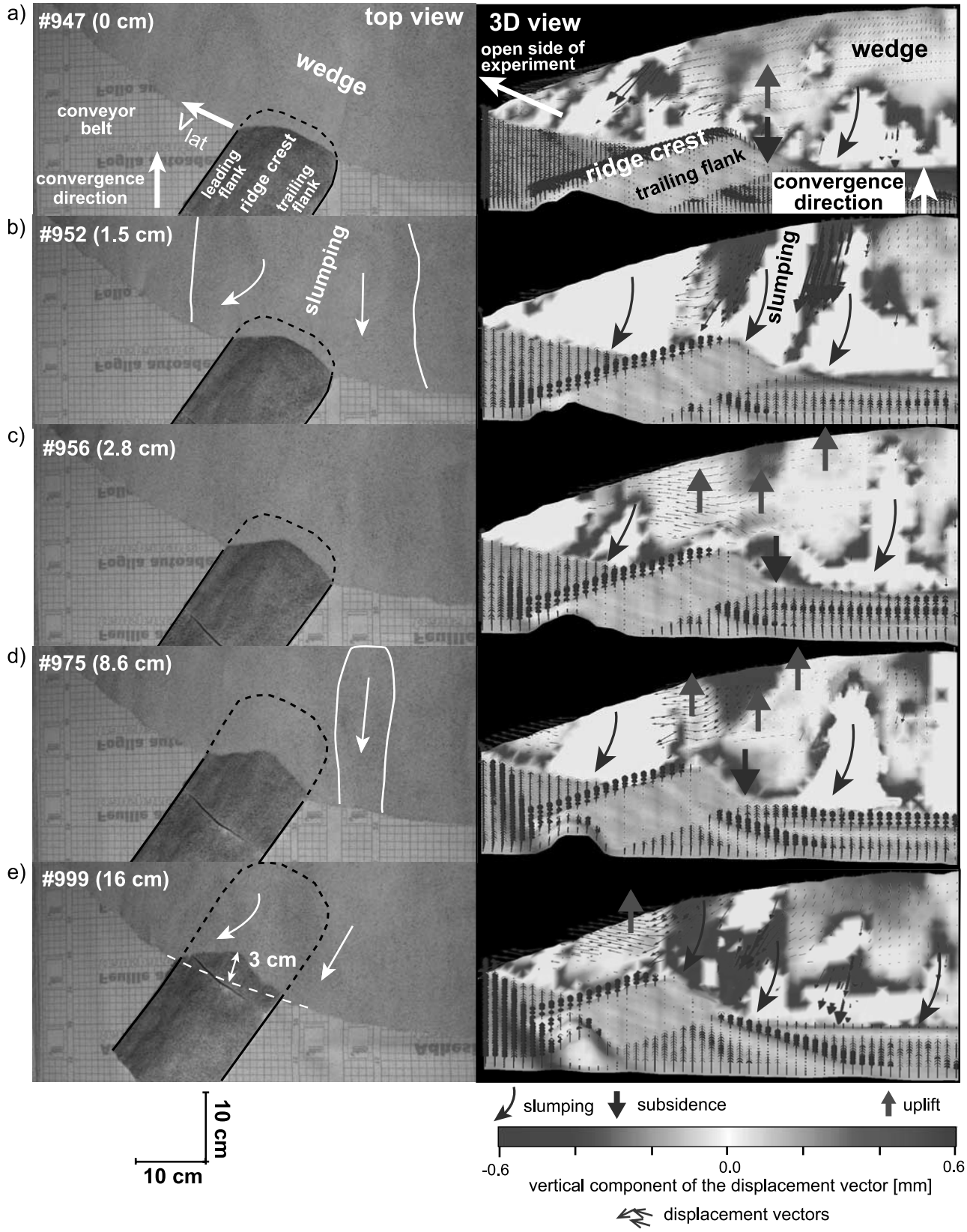
a)
#947 (0 cm)
top view
wedge
conveyor belt
v lat
convergence direction
leading flank
ridge crest
trailing flank
3D view
open side of experiment
wedge
ridge crest
trailing flank
convergence direction
b)
#952 (1.5 cm)
slumping
slumping
c)
#956 (2.8 cm)
d)
#975 (8.6 cm)
e)
#999 (16 cm)
3 cm
10 cm
10 cm
slumping
subsidence
uplift
-0.6
0.0
0.6
vertical component of the displacement vector [mm]
displacement vectors

Figure 3

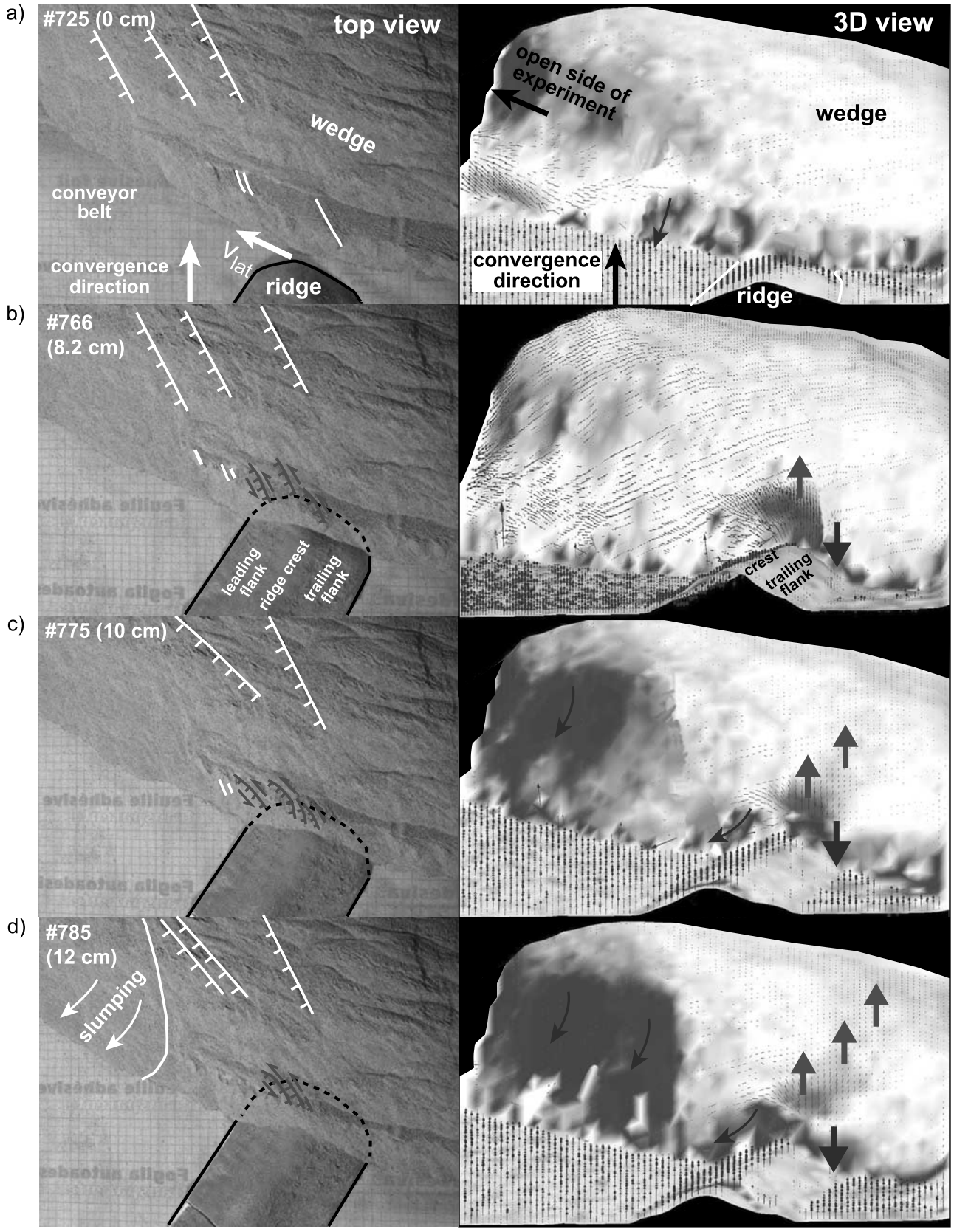
a)
#725 (0 cm)
top view
wedge
conveyor belt
convergence direction
V_{lat}
ridge
3D view
open side of experiment
wedge
convergence direction
ridge
b)
#766 (8.2 cm)
leading flank
ridge crest
trailing flank
crest
trailing flank
c)
#775 (10 cm)
d)
#785 (12 cm)
slumping

Figure 4

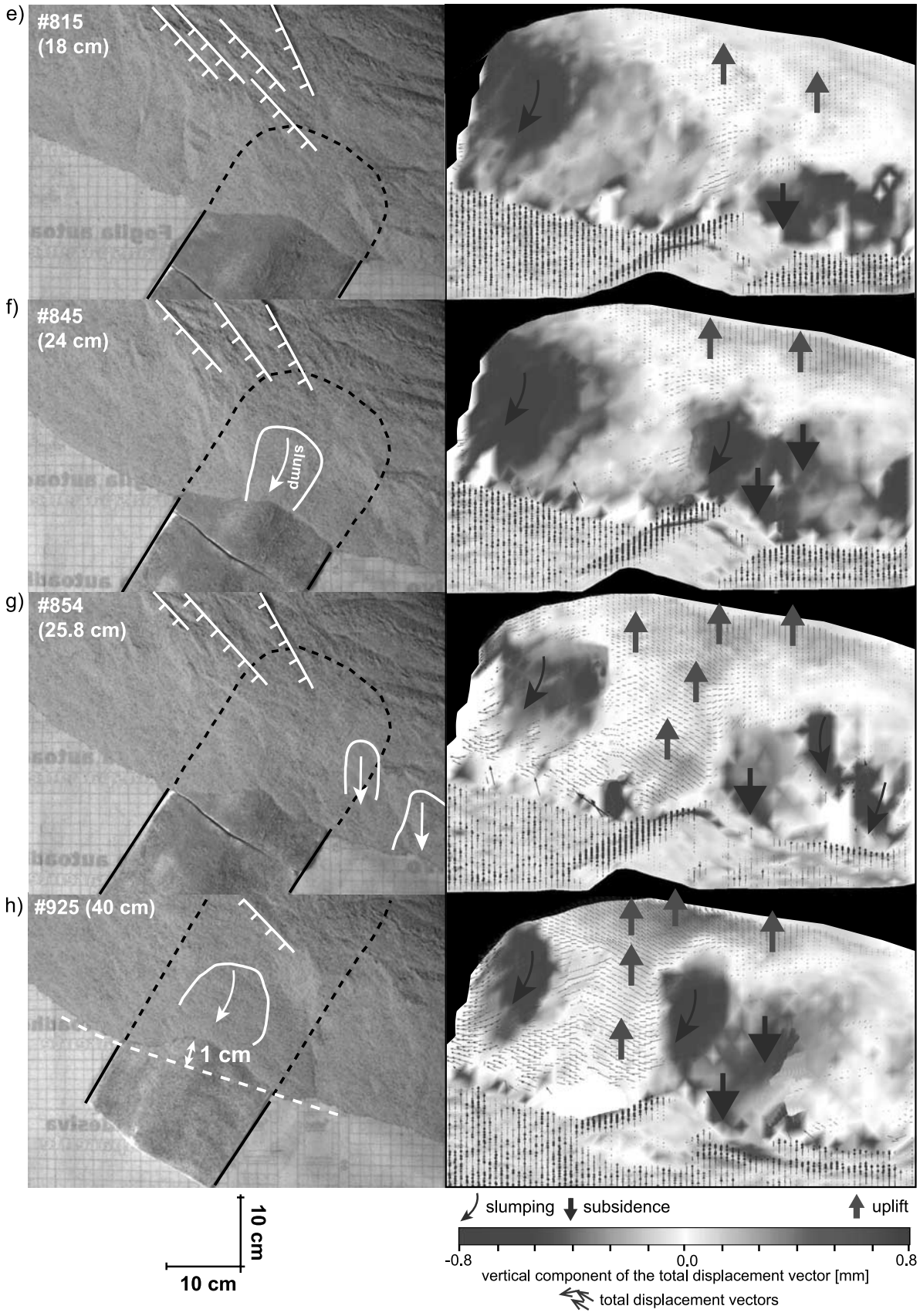

Figure 4. (continued)

these faults are difficult to extract from the PIV images as these structures mainly result from horizontal extension. Above the trailing flank of the ridge, material starts to subside without the generation of any visible faults (Figures 4b–4h, right column).

[21] As the ridge is dragged deeper underneath the wedge, the amount of uplift increases to a maximum of ~2.5 cm (not shown in figure), whereas the uplift of the wedge gradually propagates toward the back wall (Figures 4c–4h, right column). Eventually, uplift leads to oversteepening of the slope and thus ridge-induced slumps occur at the lower slope, above the leading ridge flank (Figure 4c, right column).

[22] Whereas the region of maximum uplift is located above the ridge crest during the initial stages of the experiment, it shifts toward the leading flank of the ridge in the later stages. Therefore slumping triggered by the ridge originates mainly above the leading edge and gradually affects higher parts of the slope (Figures 4d, 4f, and 4h, right column). Furthermore, the ridge crest causes a gradually increasing indentation of the wedge, resulting in a ~1-cm-deep reentrant toward the end of the experiment (Figure 4h, left column). Above the trailing flank of the ridge, the material of the lower and midslope subsides by ~2.5 cm at a rate of ~0.05 cm/s (Figures 4b–4h, right column). Slumping here occurs less frequently than above the uplifted leading flank.

5. Discussion

[23] The two 3-D sandbox experiments designed to shed light on the impact of a subducting ridge on an erosive forearc successfully provided information on the deformation patterns and their evolution through time associated with oblique ridge subduction. The first experiment using pure sand revealed the basic mass transfer modes, which were, however, frequently overprinted by slump events. The second model used a sand-mortar mixture of higher frictional strength and a smaller grain size and achieved a much better preservation of structures as well as a higher spatial resolution. For both experiments, the displacement monitoring and 3-D deformation analysis with image correlation significantly improved the detection and identification of ridge-related effects compared to the observation by naked eye, photo or video camera. Especially for the second experiment, PIV yielded excellent high-resolution data of the 3-D displacement field of the deforming wedge surface.

[24] In the following, the experimental results will be compared to geological observations in the south Peruvian forearc currently affected by the subduction of the Nazca Ridge. Analysis of the PIV images shows that the 3-cm-high ridge causes maximum uplift of ~1 cm and ~2.5 cm at rates of ~0.02 cm/s and ~0.05 cm/s in the first and second experiment, respectively, with 1 cm being equivalent to 1 km in nature (Table 1). In order to compare the model results to the collision of the 1.5-km-high Nazca Ridge, these values must be divided by two, since the model ridge is twice as high as the Nazca Ridge. This yields ~0.5 km and ~1.2 km of uplift for the first and second experiment, respectively. Secondly, to compare the uplift rates, the model convergence rate must be calibrated with the convergence velocity of the Nazca Plate. The natural convergence rate is 6.8 cm/yr, i.e., 68 km/Myr, at 17°S [*Norabuena et al.*, 1998]. Using this value, ~36 s in the models are equivalent to 1 Ma in nature. The rates of uplift in the first and second experiment can thus be converted into uplift rates of ~0.35 km/Myr and ~0.9 km/Myr, respectively (Figure 5 and Table 1). It should be noted that the uplift in the experiments is caused by the relief of the underthrusting ridge. A potential rise of the forearc owing to an isostatic adjustment related to a buoyant Nazca Ridge is not included in the sandbox experiments. For the following reasons, however, isostatic forearc uplift does not seem to contribute significantly to the pattern of uplift observed in south Peru. Numerical models, which have considered the amount and distribution of uplift as if it were solely induced by the buoyancy of the Nazca Ridge, have predicted that the maximum uplift of 800 m would occur ~100 km landward of the coast in continuation of the ridge crest, whereas the coast experiences 600–700 m of uplift [*Moretti*, 1983]. Toward the trench, forearc uplift would decrease to zero [*Moretti*, 1983]. Furthermore, an elliptic and symmetric distribution of forearc uplift with respect to the crest of the Nazca Ridge should be observed according to these models [*Moretti*, 1983; *Moretti and Ngokwey*, 1985]. More recent geologic observations reported from south Peru, however, indicate a different uplift pattern above the Nazca Ridge. Ridge-induced uplift is highest offshore (1.5 km), reaches 900–1000 m at the coast and decreases onshore until its signal disappears ~50 km from the coast (Figure 1) [*Hsu*, 1992; *Macharé and Ortlieb*, 1992; *Hagen and Moberly*, 1994; *Li and Clark*, 1994; *Hampel et al.*, 2004]. Also forearc uplift above the symmetric Nazca Ridge is distributed asymmetrically with respect to the crest [*Hsu*, 1992; *Macharé and Ortlieb*, 1992]. An alternative geometric 3-D model [*Hsu*, 1992], which neglects isostasy and explains the uplift pattern by both the relief of the ridge and its lateral motion, is more compatible with these geological observations in south Peru. In addition, marine gravimetric data do not show a free-air anomaly associated with the

Figure 4. Image sequence of the second experiment with the sand-mortar mixture showing the collision and lateral migration of the model ridge (left column) and the displacement field derived from PIV analysis in a perspective view (right column). The viewpoint toward the wedge from behind the ridge is depicted in Figure 2a. Refer to Figure 3 for explanation on PIV images and color codes (the length of the total displacement vectors is 15 times the displacement for the second model). The convergence between images 725 and 925 is ~40 cm. Note the ridge-induced normal faults with minor strike-slip component in the lowermost wedge; these faults are only visible in the initial stages of the experiment and later overprinted by slump events (Figures 4b–4e; marked in red). Gravity-induced normal faults occur near the back wall toward the open side of the experiment. See color version of this figure at back of this issue.

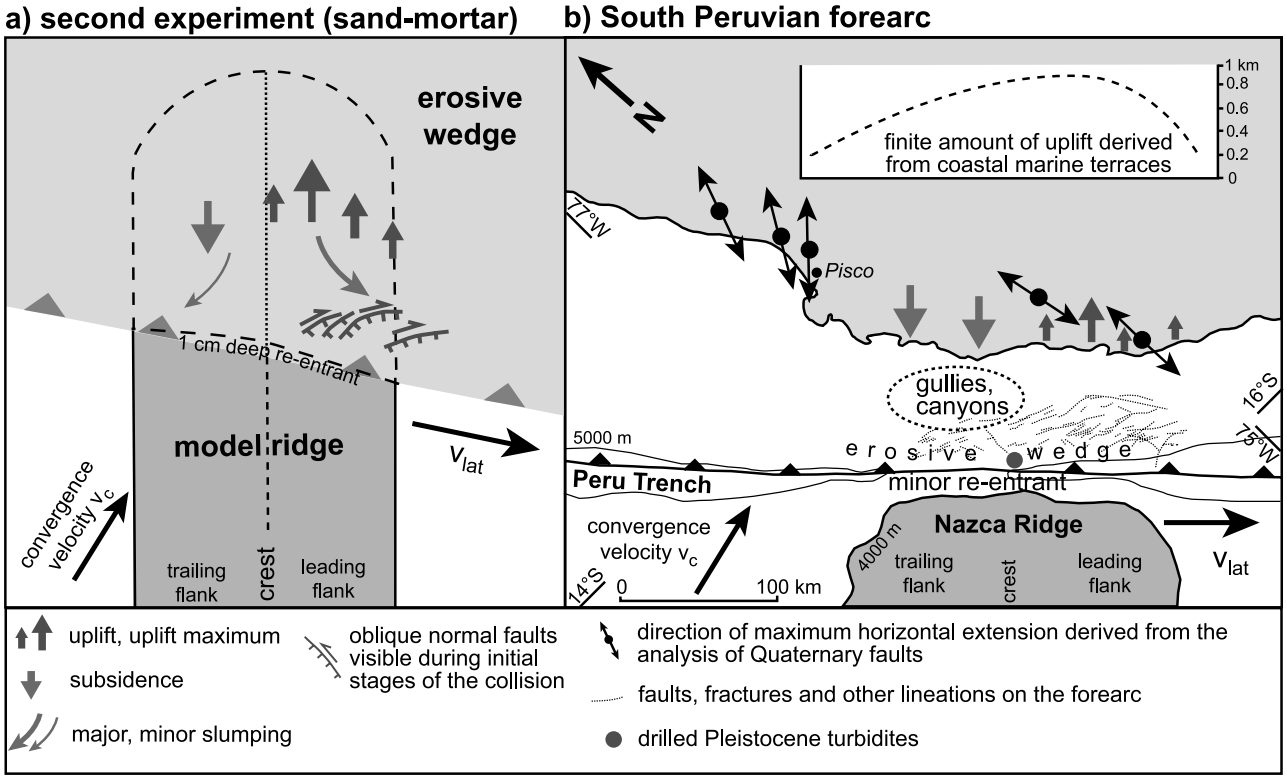

Figure 5. (a) Schematic sketch illustrating the spatial-temporal sequence of effects caused by the model ridge in the second sandbox experiment (top view). (b) Map of the collision zone of the Nazca Ridge and the south Peruvian forearc with elevation of coastal marine terraces (inset; after *Macharé and Ortlieb* [1992]). Variable horizontal extension directions above the ridge have been derived from Quaternary normal faults onshore [*Sébrier et al.*, 1985, 1988]. Lineations in the submarine part of the forearc have been inferred from side-scan sonar data [*Hagen and Moberly*, 1994]. Drilled Pleistocene turbidites suggest slumping events during the passage of the ridge [*Kulm et al.*, 1974]. Surficial mass wasting is indicated by gullies and canyons observed in bathymetric and side-scan sonar data [*Hagen and Moberly*, 1994; *Hampel et al.*, 2004]. See color version of this figure at back of this issue.

Nazca Ridge [*Couch and Whitsett*, 1981; *Heinbockel*, 2003; *Hampel et al.*, 2004]. The same data indicate free-air anomalies ~0 mGal close to the coast [*Heinbockel*, 2003; *Hampel et al.*, 2004], which argues against the isostatic adjustment as the cause of the strong uplift observed along the south Peruvian coast. On the basis of this evaluation, ridge-related isostatic uplift in the foremost south Peruvian forearc appears to be negligible. Instead, the forearc topography directly reflects the relief of the subducting Nazca Ridge. This provides the basis for a direct comparison

Table 1. Comparison of the Phenomena Observed in the 3-D Sandbox Models and in the South Peruvian Forearc

Experiment 2 (Sand-Mortar)[a]	South Peruvian Forearc	References
Subduction of 3 cm (3 km) high model ridge	Subduction of 1.5 km high Nazca Ridge	
Asymmetric distribution of uplift with maximum above leading ridge flank	Maximum uplift of marine terraces occurs south of the inland projection of the crest of the Nazca Ridge (see Figure 5)	*Hsu* [1992]; *Macharé and Ortlieb* [1992]
Maximum uplift of ~2.5 cm (2.5 km, *1.2 km*); ratio of uplift/ridge height of 0.6; uplift rate of 0.05 cm/s (1.8 km/Myr, *0.9 km/Myr*)	Maximum uplift of 0.9 km; ratio of uplift/ridge height of 0.8; uplift rate of 0.5–0.7 km/Myr	*Hsu* [1992]; *Macharé and Ortlieb* [1992]
Minor reentrant of ~1 cm (1 km)	Minor reentrant (<2 km)	
Oblique normal faults	Normal faults at coast, radial extension faults and fractures (side-scan sonar data)	*Sébrier et al.* [1985, 1988]; *Hagen and Moberly* [1994]
Oversteepening of slope, slumping	Steepest lower slope off Peru (9°–10°)	*Bialas and Kukowski* [2000]
Slumping more frequent above leading than trailing ridge flank	Quaternary slumping inferred from drilling	*Kulm et al.* [1974]

[a]Values in parentheses represent equivalent values in nature calculated with the scaling factor of 10^5; italic numbers are amount and rate of uplift normalized to height of Nazca Ridge.

between the relief of the model ridge and of the Nazca Ridge.

[25] The marine terraces that developed along the south Peruvian coast above the Nazca Ridge have been raised by up to ~900 m. Because of the limitations inherent in the applied dating methods and the ambiguities arising from correlating the various terrace levels with sea level high stands, the inferred uplift rates of 0.5 km/Myr [*Hsu*, 1992] and 0.7 km/Myr [*Macharé and Ortlieb*, 1992] are not too well constrained. Nevertheless, the presently available data suggests that the second experiment with the higher amount and rate of uplift compares better with the natural observations (Table 1). This is further illustrated by the ratio between the total amount of uplift and the height of the ridge. The uplift-to-height ratio is 0.8 for the second experiment, which is similar to a ratio of 0.6 for the Nazca Ridge whereas the first experiment yields a much lower ratio of 0.3. The mechanically stronger sand-mortar mixture is thus more appropriate to model the rocks of the south Peruvian forearc, which possess high seismic velocities and densities [*Bialas and Kukowski*, 2000; *Heinbockel*, 2003; *Hampel et al.*, 2004].

[26] The influence of the wedge strength on the style of deformation is further illustrated by comparing the reentrants observed in the two models and induced by the Nazca Ridge. Whereas for the pure sand wedge the indentation starts at the onset of collision and results in a final ~3-cm-deep reentrant, indentation of the sand-mortar wedge is minor in the initial phase of the collision and does not exceed 1 cm at the end of the experiment (cf. Figures 3 and 4a–4h; Table 1). This suggests that both, the depth and temporal evolution of a ridge-induced reentrant depend on the mechanical strength of the wedge. Again, the second experiment better reflects the situation at the collision zone where a reentrant as wide as the Nazca Ridge is absent (Figures 1 and 5). The experiments and the natural observations indicate that material of high strength near the trench prohibits a deep indentation of the wedge by the ridge.

[27] The sandbox models suggest that the passage of the ridge induces a significant change in the morphology of the slope because of enhanced surface erosion and oblique normal faulting (Figure 5). To compare the experiments and nature in detail, high-resolution data on the surface morphology of the Peruvian forearc would be desirable, but only few data are available (Figure 5b). From SeaMARC II side-scan sonar images, increased surface erosion due to the ridge has been inferred from the presence of canyons, gullies, and slump masses [*Hagen and Moberly*, 1994; *Li and Clark*, 1994]. Enhanced tectonic erosion during and after ridge passage has also been inferred from the bathymetric data of SEAMARC II and GEOPECO [*Hampel et al.*, 2004]. No data, however, are available to test if the slump events off south Peru [*Kulm et al.*, 1974] originate more frequently above the leading than above the trailing flank of the ridge, as observed in the experiments.

[28] With regard to faulting, the slightly oblique normal faults observed in the second model are in general accordance with Quaternary normal faulting observed in south Peru. The normal faults observed onshore near the Peruvian coast show variable trends and have been interpreted to indicate horizontal extension in the forearc above the Nazca Ridge (Figure 5) [*Sébrier et al.*, 1985, 1988]. Striations on these fault planes are down dip and do not show any strike-slip components. We speculate that the small lateral offsets shown by the oblique normal faults in experiment 2 are due to facilitated material movement toward the open side of the experiment. Offshore, side-scan sonar images show linear features that have been interpreted as faults and fractures, which existed prior to the arrival of the Nazca Ridge and may be active as strike-slip faults during the ridge passage (Figure 5b) [*Hagen and Moberly*, 1994]. Despite the differences in their length, the faults observed in the experiment shortly after the onset of the collision show affinities with these features. Moreover, only minor contractional deformation occurs in south Peru [*Hagen and Moberly*, 1994], which agrees with the absence of thrust faulting and the lack of a deep reentrant in both, experiment and nature.

[29] The modeled temporal sequence of ridge-induced uplift and subsidence of the wedge with the maximum uplift being offset relative to the crest toward the motion direction of the ridge, is in agreement with the observations at the collision zone (Figure 5b and Table 1). The south Peruvian marine terraces document strong uplift above the southeastern flank of the Nazca Ridge, whereas the coast above and north of the ridge crest experiences moderate uplift and net subsidence, respectively [*Hsu*, 1992; *Macharé and Ortlieb*, 1992]. As in the experiments, the maximum amount of uplift occurs south of the inland projection of the ridge crest, i.e., above its leading edge. The noncoincidence between the location of the uplift maximum and the highest point of the ridge has been attributed to the oblique subduction of the ridge [*Hsu*, 1992; *Macharé and Ortlieb*, 1992]. The analogue models support this explanation and additionally suggest that, at the onset of collision, the highest uplift occurs close to the ridge crest and only later shifts away from the crest. This leads to an increasing asymmetry in the spatial distribution of uplift with respect to the ridge axis (Figures 4a–4h). A close relationship between the uplift distribution and the obliquity of the ridge subduction is supported by two other ridges. Bathymetric data of the Louisville Ridge, which migrates southward along the erosive Tonga-Kermadec margin, show that the highest forearc uplift occurs above the leading flank of ridge [*Ballance et al.*, 1989]. In contrast, the Cocos Ridge, which is parallel to the convergence direction of the Cocos Plate and does not migrate along the Panama-Costa-Rican margin, causes uplift that that is almost symmetric with respect to its crest [*Gardner et al.*, 1992; *Corrigan et al.*, 1990].

[30] The two experiments we performed show profound differences to the 3-D sandbox models and the geological record of the accretive Ryukyu margin, where the 2-km-high Gagua Ridge is obliquely subducted [*Schnuerle et al.*, 1998; *Dominguez et al.*, 1998]. The collision zone of the Gagua Ridge shows a deep indentation of the ~60-km-wide accretionary prism. The reentrant has a similar width as the ridge and is highly asymmetric with respect to the ridge axis [*Dominguez et al.*, 1998]. The collision of the ridge results in a compressional state of stress that induces conjugate strike-slip faults, which diverge from the ridge crest to the

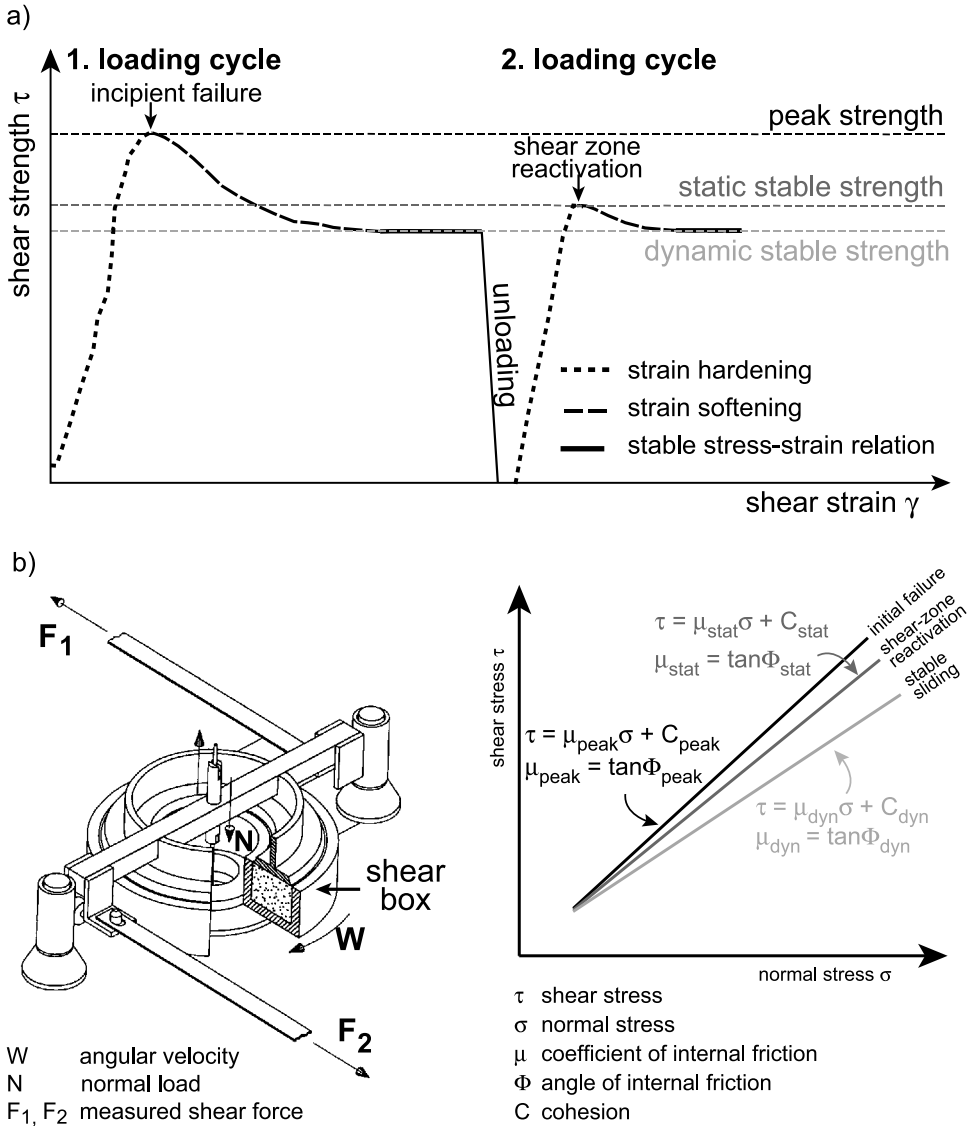

Figure A1. (a) Characteristic stress-strain curve for analogue materials. (b) Setup of the ring-shear device [*Schulze*, 1994] used to measure the relation between shear and normal stresses during loading of the analogue material from which internal friction and cohesion are determined by linear regression.

NW and NE. This divergent fault network, has been recognized in both, bathymetric data and sandbox models [*Dominguez et al.*, 1998], and differs significantly from the one inferred for the south Peruvian forearc.

[31] We propose that these fundamental differences in the deformation of the upper plate at the Peruvian and Ryukyu margins arise from the different long-term mass transfer regimes that have acted upon their forearc systems. At accretive margins, mechanically weak sediments are offscraped from the oceanic plate and accreted against a less deformable buttress, which may be formed by older accreted material, arc-derived intrusives, or older basement rocks [e.g., *Scholl et al.*, 1980; *von Huene and Scholl*, 1991]. In contrast, at erosive margins, any weak sediment that might have been accreted earlier is removed on long timescales. As a consequence, mechanically strong crystalline rocks are gradually transferred toward the trench in a passive manner [*von Huene and Lallemand*, 1990; *von Huene and Scholl*, 1991; *Clift and MacLeod*, 1999; *Vanneste and Larter*, 2002]. Thus the strength of a forearc and its response to a colliding bathymetric high will depend on whether long-term accretion or tectonic erosion has taken place along the margin in the past.

6. Conclusions

[32] The second one of our 3-D models, which used a mechanically strong material, is in good agreement with geological observations at the collision zone of the Nazca Ridge in southern Peru, where strong crystalline rocks are present close to the trench. In both, model and nature, the

Table A1. Coefficients of Internal Friction, Angles of Internal Friction, and Cohesion Values of the Analogue Materials Derived From the Measurements With a Ring Shear Apparatus

	Peak Friction			Static-Stable Friction			Dynamic-Stable Friction		
Density, kg/m^3	Internal Friction μ_{peak}	Angle of Internal Friction φ_{peak}	Cohesion C_{peak}, Pa	Internal Friction μ_{stat}	Angle of Internal Friction φ_{stat}	Cohesion C_{stat}, Pa	Internal Friction μ_{dyn}	Angle of Internal Friction φ_{dyn}	Cohesion C_{dyn}, Pa
1:1 Mixture of Dry Quartz Sand (Grain Size <0.4 mm) and Dry Mortar									
1656	0.76	37.1°	6[a]	0.70	34.8°	31	0.62	31.6°	51
±16	±0.02	±0.7	±19	±0.10	±0.3	±6	±0.002	±0.1	±3
Dry Quartz Sand (Grain Size <0.63 mm)									
1732	0.73	36.2°	64	0.60	31.0°	90	0.57	29.6°	67
±8	±0.01	±0.3	±20	±0.002	±0.1	±7	±0.002	±0.1	±5

[a]Note that cohesion is determined by linear regression analysis; thus, for cohesion values close to zero, statistical fluctuation lead to apparently negative values.

ridge does not deflect the lower part of the wedge. Above the ridge, normal faults develop in the wedge. Because of the obliquity of subduction the maximum uplift does not coincide with the ridge crest, but occurs above the leading flank of the ridge. In the wake of the ridge, the forearc undergoes subsidence.

[33] The models and a comparison of natural convergent margins indicate that, in contrast to accretive margins, erosive margins undergoing ridge subduction are generally characterized by a minor reentrant, resulting from a mechanically strong frontal wedge. The presence of mechanically strong rocks in the forearc can be explained by long-term tectonic erosion, a process that causes continental basement to shift passively toward the trench. Thus the main response of erosive margins to ridge subduction is inferred to be forearc uplift accompanied by horizontal extension, whereas at accretive margins, deformation caused by horizontal shortening prevails.

Appendix A: Model Scaling and Frictional Properties of the Analogue Materials

[34] In order to be directly comparable to natural settings, the experiment and the analogue material must be scaled to nature with respect to their length units, density and frictional properties, respectively [*Hubbert*, 1937; *Schellart*, 2000]. This is expressed in the following relationship:

$$C_{\text{model}}/C_{\text{nature}} = (\rho g\, x)_{\text{model}}/(\rho g\, x)_{\text{nature}},$$

where C is cohesion, ρ is density, g is acceleration of gravity, and x is length units [*Hubbert*, 1937; *Schellart*, 2000]. Note that gravity does not need to be scaled if cohesion, density, and length units scale down appropriately. The scaling factor of models carried out under normal gravity can be calculated by $(C/\rho g)_{\text{nature}}/(C/\rho g)_{\text{model}}$ [*Hubbert*, 1937; *Koyi*, 1997; *Schellart*, 2000]. Scaling of the sandbox experiments requires the frictional properties of the analogue material to be measured. Analogue materials with deformation behaviors similar to brittle upper crustal rocks are sand and sand-mortar mixtures, which show a Mohr-Coulomb behavior with strain hardening and softening before and after failure, respectively [*Byerlee*, 1978; *Mandl*, 1988; *Marone*, 1998; *Krantz*, 1991; *Schellart*, 2000; *Lohrmann et al.*, 2003]. Both, sand and upper crustal rocks, tend to localize deformation, i.e., the frictional strength along faults is reduced compared to the undeformed material [*Byerlee*, 1978]. Frictional strength is defined by the peak friction of the undeformed material, the static-stable friction for the strength of previously deformed material (shear zone reactivation) and the dynamic-stable friction for the strength of active shear zones [*Byerlee*, 1978] (Figure A1).

[35] We used a ring shear apparatus to measure the peak, static-stable, and dynamic-stable frictions of our analogue materials (Figure A1). During each measurement set, normal loads between 1–12 kg are applied to the material in the ring shear apparatus (Figure A1). These loads are of the same order of magnitude as the loads the material experiences during an experiment. In the first loading cycle, the undeformed material is sheared and the occurring shear forces are recorded (Figure A1). In the following unloading phase, the rotation direction is reversed until the shear strength drops to zero. At this moment, the rotation direction is again reversed for a second loading cycle, in which the shear zone is reactivated (Figure A1). This whole procedure is carried out three times to assess the error of the measured values. Friction coefficients and cohesion are calculated by linear regression (Figure A1) and listed in Table 1. The standard errors of the angles of internal friction do not exceed 4% throughout. The cohesion of the material is negligible (<100 Pa), since the normal stresses observed in the experiments reach up to 6000 Pa. Inserting the mean cohesion and density values of the analogue and natural materials into the relationship $[C/\rho g]_{\text{nature}}/[C/\rho g]_{\text{model}}$ yields a scaling factor of $\sim 10^5$ for the experiments.

[36] **Acknowledgments.** The experiments have been carried out in the Geodynamics Laboratory of the GeoForschungsZentrum Potsdam. We thank O. Oncken, J. Lohrmann, and S. Hoth for fruitful discussions and G. Tauscher for technical assistance. B. Wieneke and K. Pfeiffer of LaVision GmbH Goettingen provided valuable technical support for the used PIV system. A. H. wishes to thank R. Hetzel for thorough and thoughtful criticism on several earlier versions of the manuscript. Associate Editor L. Ratschbacher, I. Moretti, C. Talbot, and an anonymous reviewer provided careful and constructive reviews. Funding to A. H. and J. A. was provided by the Deutsche Forschungsgemeinschaft (DFG) through a grant (Leibniz-Program) to O. Oncken.

References

Adam, J., J. L. Urai, B. Wieneke, O. Oncken, K. Pfeiffer, N. Kukowski, J. Lohrmann, W. van der Zee, and J. Schmatz (2004), Shear localisation and strain distribution during tectonic faulting—New insights from granular-flow experiments and high-resolution optical image correlation techniques, *J. Struct. Geol.*, in press.

Ballance, P. F., D. W. Scholl, T. L. Vallier, A. J. Stevenson, H. Ryan, and R. H. Herzer (1989), Subduction of a Late Cretaceous seamount of the Louisville Ridge at the Tonga Trench: A model of normal and accelerated tectonic erosion, *Tectonics*, *8*, 953–962.

Bialas, J., and N. Kukowski (2000), Geophysical experiments at the Peruvian continental margin: Investigations of tectonics, mechanics, gas hydrates and fluid transport, *GEOMAR Rep. 96*, Geomar, Kiel, Germany.

Broggi, J. A. (1946), Las terrazas marinas de la Bahia de San Juan en Ica, *Bol. Soc. Geol. Peru*, *19*, 21–33.

Burbridge, D. R., and J. Braun (1998), Analogue models of obliquely convergent continental plate boundaries, *J. Geophys. Res.*, *103*(B7), 15,221–15,237.

Byerlee, J. (1978), Friction of rocks, *Pure Appl. Geophys.*, *116*, 615–626.

Clift, P. D., and C. J. MacLeod (1999), Slow rates of subduction erosion estimated from subsidence and tilting of the Tonga forearc, *Geology*, *27*, 411–414.

Clift, P. D., I. Pecher, N. Kukowski, and A. Hampel (2003), Tectonic erosion of the Peruvian forearc, Lima Basin, by subduction and Nazca Ridge collision, *Tectonics*, *22*(3), 1023, doi:10.1029/2002TC001386.

Collot, J.-Y., and B. Davy (1998), Forearc structures and tectonic regimes at the oblique subduction zone between the Hikurangi Plateau and the southern Kermadec margin, *J. Geophys. Res.*, *103*(B1), 623–650.

Corrigan, J., P. Mann, and J. C. Ingle (1990), Forearc response to subduction of the Cocos Ridge, Panama-Costa Rica, *Geol. Soc. Am. Bull.*, *102*, 628–652.

Couch, R., and R. M. Whitsett (1981), Structures of the Nazca Ridge and the continental shelf and slope of southern Peru, in *Nazca Plate: Crustal Formation and Andean Convergence*, edited by L. D. Kulm et al., *Mem. Geol. Soc. Am.*, *154*, 569–586.

Dahlen, J. S. F. (1984), Non-cohesive Critical Coulomb wedges: An exact solution, *J. Geophys. Res.*, *89*(B12), 10,125–10,133.

Davis, D. M., J. Suppe, and J. S. F. Dahlen (1983), Mechanics of fold-and-thrust belts and accretionary wedges, *J. Geophys. Res.*, *88*(B2), 1153–1172.

Dominguez, S., S. Lallemand, J. Malavieille, and P. Schnuerle (1998), Oblique subduction of the Gagua Ridge beneath the Ryukyu accretionary wedge system: Insights from marine observations and sandbox experiments, *Mar. Geophys. Res.*, *20*, 383–402.

Fincham, A. M., and G. R. Spedding (1997), Low cost high resolution DPIV for measurement of turbulent fluids, *Exp. Fluids*, *23*, 449–462.

Gardner, T. W., D. Verdonck, N. M. Pinter, R. Slingerland, K. P. Furlong, T. F. Bullard, and S. G. Wells (1992), Quaternary uplift astride the aseismic Cocos Ridge, Pacific coast, Costa Rica, *Geol. Soc. Am. Bull.*, *104*, 219–232.

Gutscher, M.-A., N. Kukowski, J. Malavieille, and S. Lallemand (1996), Cyclical behavior of thrust wedges: Insights from high basal friction sandbox experiments, *Geology*, *24*, 135–138.

Gutscher, M.-A., J. Malavieille, S. Lallemand, and J.-Y. Collot (1999), Tectonic segmentation of the North Andean margin: Impact of the Carnegie Ridge collision, *Earth Planet. Sci. Lett.*, *168*, 255–270.

Hagen, R. A., and R. Moberly (1994), Tectonic effects of a subducting aseismic ridge: The subduction of the Nazca Ridge at the Peru Trench, *Mar. Geophys. Res.*, *16*, 145–161.

Hampel, A. (2002), The migration history of the Nazca Ridge along the Peruvian active margin: A re-evaluation, *Earth Planet. Sci. Lett.*, *203*, 665–679.

Hampel, A. (2003), Subduction of the Nazca Ridge at the Peruvian margin: Insights from geophysical data, analogue and numerical modelling, Ph.D. thesis, Free Univ., Berlin.

Hampel, A., N. Kukowski, J. Bialas, C. Huebscher, and R. Heinbockel (2004), Ridge subduction at an erosive margin: The collision zone of the Nazca Ridge in southern Peru, *J. Geophys. Res.*, *109*, B02101, doi:10.1029/2003JB002593.

Heinbockel, R. (2003), Gravity and magnetic investigations along the Peruvian continental margin, Staats-und Universitaets bibl. Carl von Ossietzky, Univ. of Hamburg, Hamburg, Germany. (available at http://allegro.sub.uni-hamburg.de/emedien/edissertationen/fach.html)

Hsu, J. T. (1992), Quaternary uplift of the Peruvian coast related to the subduction of the Nazca Ridge: 13.5 to 15.6 degrees south latitude, *Quat. Int.*, *15/16*, 87–97.

Hsu, J. T., E. Leonard, and J. F. Wehmiller (1989), Aminostratigraphy of Peruvian and Chilean marine terraces, *Quat. Sci. Rev.*, *8*, 292–297.

Hubbert, M. K. (1937), Theory of scale models as applied to the study of geological structures, *Geol. Soc. Am. Bull.*, *48*, 459–1520.

Koyi, H. (1997), Analogue modeling: From a qualitative to a quantitative technique: A historical outline, *J. Pet. Geol.*, *20*, 223–283.

Krantz, R. W. (1991), Measurements of friction coefficients and cohesion for faulting and fault reactivation in laboratory models using sand and sand mixtures, *Tectonophysics*, *188*, 203–207.

Kukowski, N., R. von Huene, J. Malavieille, and S. E. Lallemand (1994), Sediment accretion against a buttress beneath the Peruvian continental margin at 12°S as simulated with sandbox modeling, *Geol. Rundsch.*, *83*, 822–831.

Kukowski, N., A. Hampel, J. Bialas, C. Huebscher, and J. Bourgois (2003), Erosive Margins: The link between the nature of oceanic plate and slope surface at the Peruvian margin and the margin's mechanical state, paper presented at EGS-EUG-AGU Joint Assembly, Nice, France.

Kulm, L. D., J. M. Resig, T. C. Moore, and V. J. Rosato (1974), Transfer of Nazca Ridge pelagic sediments to the Peru continental margin, *Geol. Soc. Am. Bull.*, *85*, 769–780.

Kulm, L. D., J. Dymond, E. J. Dasch, and D. M. Hussong (1981), Nazca plate: Crustal formation and Andean convergence, *Mem. Geol. Soc.*, 154.

Lallemand, S. E., J. Malavieille, and S. Calassou (1992), Effects of oceanic ridge subduction on accretionary wedges, experimental modeling and marine observations, *Tectonics*, *11*, 1301–1313.

Lallemand, S. E., P. Schnuerle, and J. Malavieille (1994), Coulomb theory applied to accretionary and non-accretionary wedges: Possible causes for tectonic erosion and/or frontal accretion, *J. Geophys. Res.*, *99*(6), 12,033–12,055.

Le Roux, J. P., C. Tavares Correa, and F. Alayza (2000), Sedimentology of the Rímac-Chillón alluvial fan at Lima, Peru, as related to Plio-Pleistocene sea level changes, glacial cycles and tectonics, *J. S. Am. Earth Sci.*, *13*, 499–510.

Li, C., and A. L. Clark (1994), Tectonic effects of the subducting Nazca Ridge on the southern Peru continental margin, *Mar. Pet. Geol.*, *11*(5), 575–586.

Liu, J. Y., and G. Ranalli (1992), Stresses in an overthrust sheet and propagation of thrusting: An airy stress function solution, *Tectonics*, *11*, 549–559.

Lohrmann, J., N. Kukowski, J. Adam, and O. Oncken (2003), The impact of analogue material properties on the geometry, kinematics, and dynamics of convergent sand wedges, *J. Struct. Geol.*, *25*(10), 1691–1711.

Macharé, J. (1987), La marge continentale du Pérou: Régimes tectonique et sédimentaires cénozoiques de l'avant-arc des Andes centrales, thèse Doct. Sc., 391 pp. Univ. Paris XI, Paris.

Macharé, J., and L. Ortlieb (1992), Plio-Quaternary vertical motions and the subduction of the Nazca Ridge, central coast of Peru, *Tectonophysics*, *205*, 97–108.

Mandl, G. (1988), *Mechanics of Tectonic Faulting: Models and Basic Concepts*, 407 pp., Elsevier Sci., New York.

Marone, C. (1998), Laboratory-derived friction laws and their application to seismic faulting, *Annu. Rev. Earth. Planet. Sci.*, *26*, 643–696.

McCaffrey, R. (1992), Oblique plate convergence, slip vectors, and fore-arc deformation, *J. Geophys. Res.*, *97*(B6), 8905–8915.

McCann, W. R., and R. E. Habermann (1989), Morphologic and geologic effects of the subduction of bathymetric highs, *Pure Appl. Geophys.*, *129*, 41–69.

Moretti, I. (1983), Subduction des rides aseismiques, thèse de 3ème cycle, 118 pp., Univ. d'Orsay, Orsay, France.

Moretti, I., and K. Ngokwey (1985). Aseismic ridge subduction and vertical motion of overriding plate, in *Géodynamique des Caraibes: Symposium, Paris*, pp. 245–253. Ed. Technip, Paris.

Mulugeta, G. (1988), Modeling the geometry of Coulomb thrust wedges, *J. Struct. Geol.*, *10*(8), 847–859.

Norabuena, E., L. Leffler-Griffin, A. Mao, T. Dixon, S. Stein, I. S. Sacks, L. Ocola, and M. Ellis (1998), Space geodetic observations of Nazca-South American convergence across the central Andes, *Science*, *279*, 358–362.

Pardo-Casas, F., and P. Molnar (1987), Relative motion of the Nazca (Farallon) and South American plates since Late Cretaceous time, *Tectonics*, *6*, 233–248.

Ranero, C. R., and R. von Huene (2000), Subduction erosion along the middle America convergent margin, *Nature*, *404*, 748–752.

Resig, J. M. (1990), Benthic foraminiferal stratigraphy and paleo-environments off Peru, leg 112, *Proc. Ocean Drill. Program Initial Rep.*, *112*, 263–296.

Scarano, F., and M. L. Riethmueller (2000), Advances in iterative multigrid PIV image processing, *Exp. Fluids*, *29*, 51–60.

Schellart, W. P. (2000), Shear test results for cohesion and friction coefficients for different granular materials: Scaling implications for their usage in analogue modeling, *Tectonophysics*, *324*, 1–16.

Schnuerle, P., C.-S. Liu, S. E. Lallemand, and D. L. Reed (1998), Structural insight into the south Ryukyu margin: Effects of the subducting Gagua Ridge, *Tectonophysics*, *288*, 237–250.

Scholl, D. W., R. von Huene, T. L. Vallier, and D. G. Howell (1980), Sedimentary masses and concepts about tectonic processes at underthrust ocean margins, *Geology*, *8*, 564–568.

Schulze, D. (1994), Entwicklung und Anwendung eines neuartigen Ringschergeraetes, *Aufbereitungstechnik*, *35*(10), 524–535.

Sébrier, M., J. L. Mercier, F. Mégard, B. Laubacher, and E. Carey-Gailhardis (1985), Quaternary normal and reverse faulting and the state of stress in the central Andes of south Peru, *Tectonics*, *4*, 739–780.

Sébrier, M., J. L. Mercier, J. Macharé, D. Bonnot, J. Cabrera, and J. L. Blanc (1988), The state of stress in an overriding plate situated above a flat slab: The Andes of central Peru, *Tectonics*, *7*, 895–928.

Smith, W. H. F., and D. T. Sandwell (1997), Global seafloor topography from satellite Altimetry and ship depth soundings, *Science*, *277*, 1956–1962.

Somoza, R. (1998), Updated Nazca (Farallon)-South America relative motions during the last 40 My:

Implications for mountain building in the Central Andean region, *J. S. Am. Earth Sci.*, *11*, 211–215.

Storti, F., and K. McClay (1995), Influence of syntectonic sedimentation on thrust wedges in analogue models, *Geology*, *23*, 999–1002.

Suess, E., et al. (1988), *Proceedings of the Ocean Drilling Program, Initial Reports*, vol. 112, Ocean Drill. Program, College Station, Tex.

Vanneste, L. E., and R. D. Larter (2002), Sediment subduction, subduction erosion, and strain regime in the northern South Sandwich forearc, *J. Geophys. Res.*, *107*(B7), 2149, doi:10.1029/2001JB000396.

von Huene, R., and S. Lallemand (1990), Tectonic erosion along the Japan and Peru convergent margins, *Geol. Soc. Am. Bull.*, *102*, 704–720.

von Huene, R., and D. W. Scholl (1991), Observations at convergent margins concerning sediment subduction, sediment erosion, and the growth of continental crust, *Rev. Geophys.*, *29*(3), 279–316.

von Huene, R., E. Suess and the Leg 112 Shipboard Scientific Party (1988), Ocean Drilling Program Leg 112, Peru continental margin, part 1, Tectonic history, *Geology*, *16*, 934–938.

von Huene, R., I. Pecher, and M.-A. Gutscher (1996), Development of the accretionary prism along Peru and material flux after subduction of Nazca Ridge, *Tectonics*, *15*, 19–33.

Wang, W.-H., and D. M. Davis (1996), Sandbox model simulation of forearc evolution and noncritical wedges, *J. Geophys. Res.*, *101*(B5), 1329–1339.

Wieneke, B. (2001), PIV adaptive multi-pass correlation with deformed interrogation windows, paper presented at First International PIV Challenge Symposium, Dtsch. Luft und Raumfahrtges. (DLR), Goettingen, Germany.

J. Adam, Department of Earth Sciences, Dalhousie University, Halifax, Nova Scotia, Canada B3J 3J5.

A. Hampel, Institute of Geological Sciences, University of Bern, Baltzerstrasse 1, CH-3012 Bern, Switzerland. (andrea@geo.unibe.ch)

N. Kukowski, GeoForschungsZentrum Potsdam, Telegrafenberg, D-14473 Potsdam, Germany.

Figure 3. Image sequence of the first experiment with pure sand showing the collision and lateral migration of the model ridge (left column) and the 3-D displacement field derived from PIV monitoring in a perspective view (right column). The viewpoint toward the wedge from behind the ridge is depicted in Figure 2a. The blue arrows in the PIV images represent the total displacement vectors (length of vectors is 20 times the displacement). The total displacement vectors are overlain on the vertical component of the displacement vector (right column; color code on model topography). Thick red and green arrows mark uplifting or subsiding areas, respectively (right column). Thin green arrows mark the parts of the slope that fail because of oversteepening (right column). In white areas without blue vectors the particles moved faster than the PIV system could trace them.

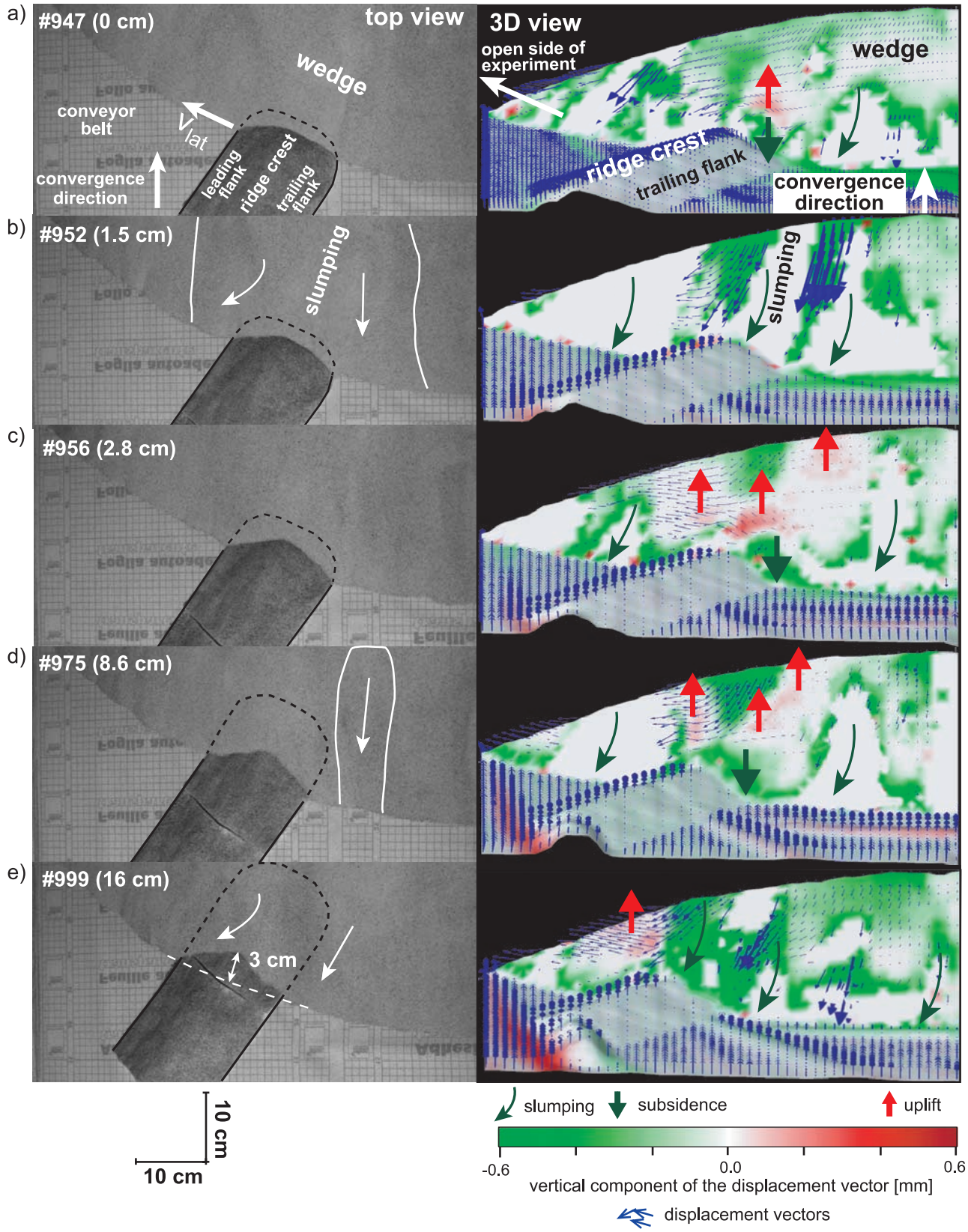
a)
#947 (0 cm)
top view
wedge
conveyor belt
v_{lat}
convergence direction
leading flank
ridge crest
trailing flank
3D view
open side of experiment
wedge
ridge crest
trailing flank
convergence direction
b)
#952 (1.5 cm)
slumping
slumping
c)
#956 (2.8 cm)
d)
#975 (8.6 cm)
e)
#999 (16 cm)
3 cm
10 cm
10 cm
slumping
subsidence
uplift
-0.6
0.0
0.6
vertical component of the displacement vector [mm]
displacement vectors

Figure 3

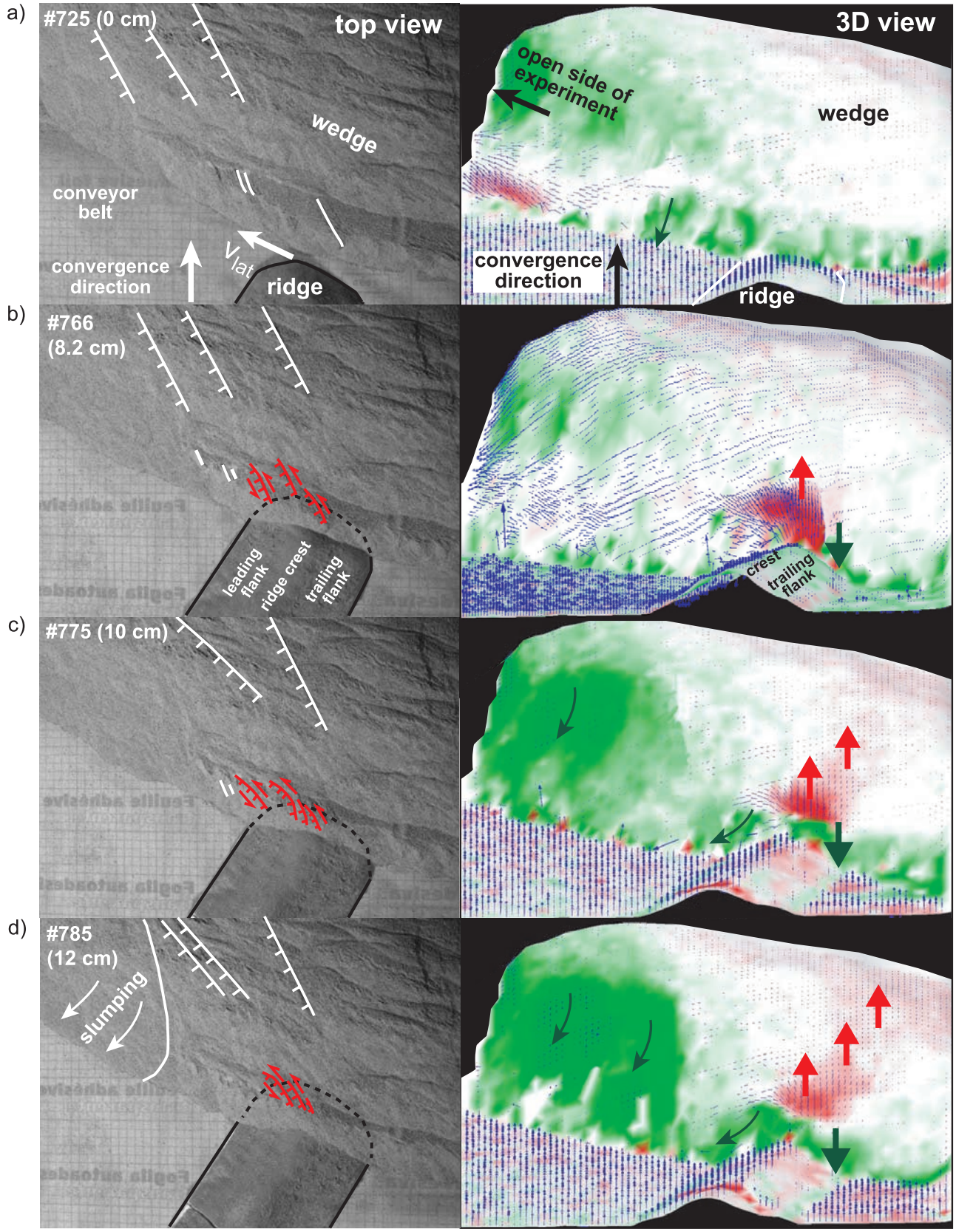
a)
#725 (0 cm)
top view
wedge
conveyor belt
convergence direction
v_{lat}
ridge
3D view
open side of experiment
wedge
convergence direction
ridge
b)
#766 (8.2 cm)
leading flank
ridge crest
trailing flank
crest
trailing flank
c)
#775 (10 cm)
d)
#785 (12 cm)
slumping

Figure 4

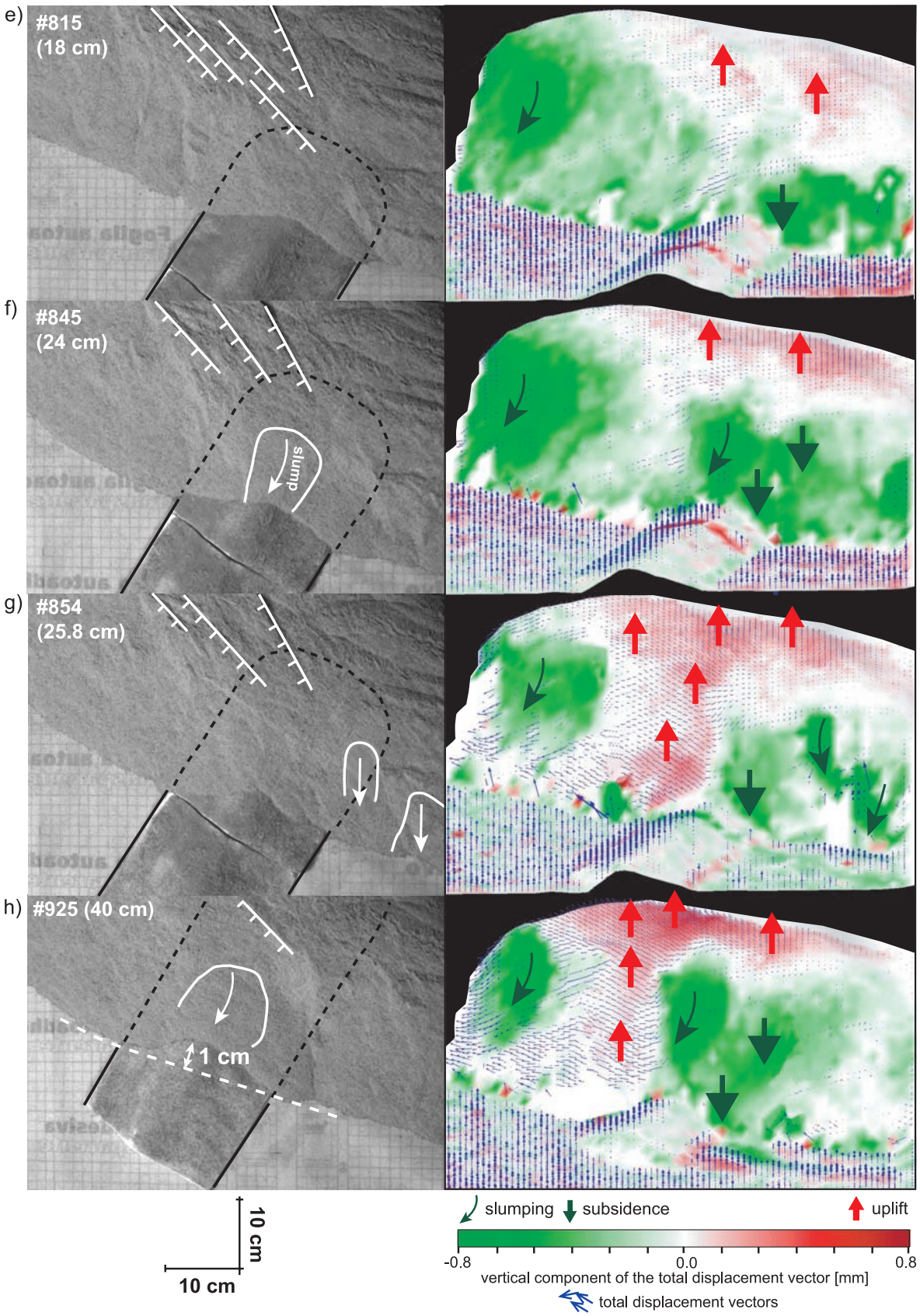

Figure 4. (continued)

Figure 4. Image sequence of the second experiment with the sand-mortar mixture showing the collision and lateral migration of the model ridge (left column) and the displacement field derived from PIV analysis in a perspective view (right column). The viewpoint toward the wedge from behind the ridge is depicted in Figure 2a. Refer to Figure 3 for explanation on PIV images and color codes (the length of the total displacement vectors is 15 times the displacement for the second model). The convergence between images 725 and 925 is ~40 cm. Note the ridge-induced normal faults with minor strike-slip component in the lowermost wedge; these faults are only visible in the initial stages of the experiment and later overprinted by slump events (Figures 4b–4e; marked in red). Gravity-induced normal faults occur near the back wall toward the open side of the experiment.

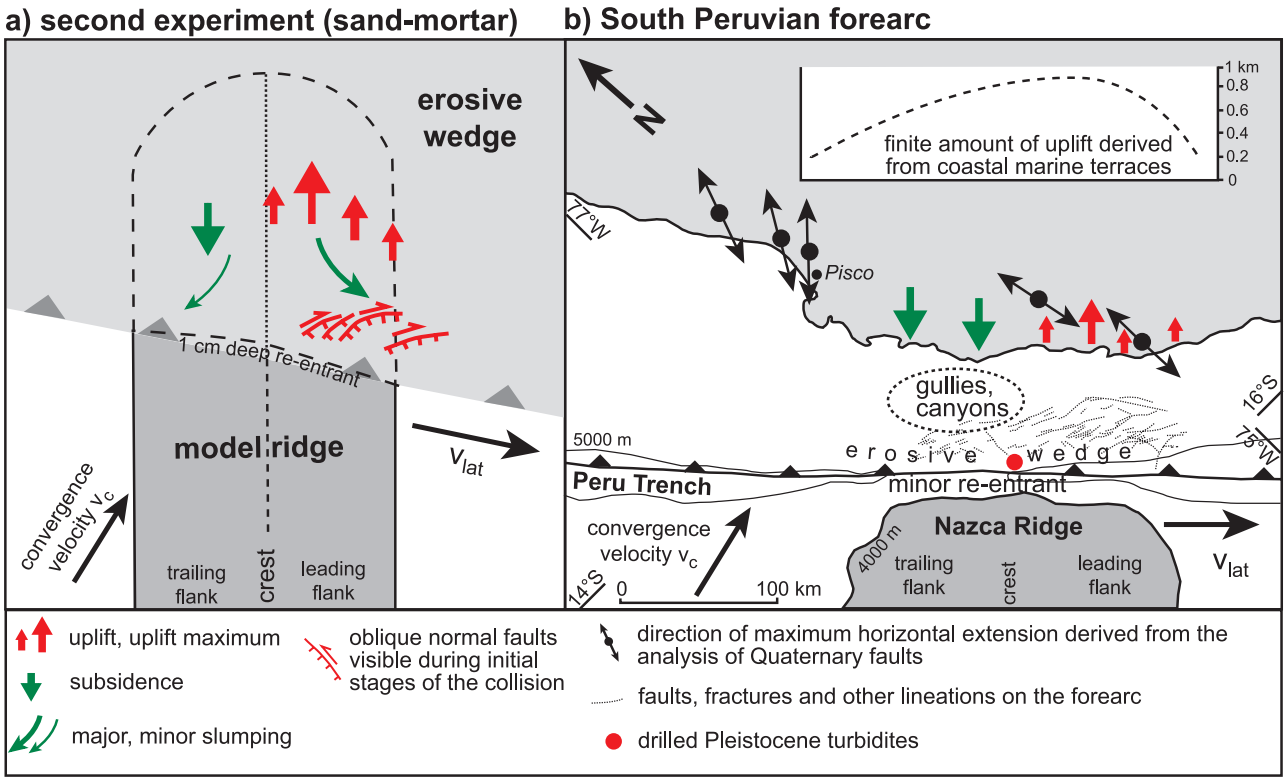

Figure 5. (a) Schematic sketch illustrating the spatial-temporal sequence of effects caused by the model ridge in the second sandbox experiment (top view). (b) Map of the collision zone of the Nazca Ridge and the south Peruvian forearc with elevation of coastal marine terraces (inset; after *Macharé and Ortlieb* [1992]). Variable horizontal extension directions above the ridge have been derived from Quaternary normal faults onshore [*Sébrier et al.*, 1985, 1988]. Lineations in the submarine part of the forearc have been inferred from side-scan sonar data [*Hagen and Moberly*, 1994]. Drilled Pleistocene turbidites suggest slumping events during the passage of the ridge [*Kulm et al.*, 1974]. Surficial mass wasting is indicated by gullies and canyons observed in bathymetric and side-scan sonar data [*Hagen and Moberly*, 1994; *Hampel et al.*, 2004].